

Article

Photonic Measurement for Doppler Frequency Shift and Angle of Arrival Based on a Dual-Polarization Dual-Drive Mach–Zehnder Modulator

Qingqing Meng ^{*} , Tao Lin, Zihang Zhu, Guodong Wang, He Li, Xuan Li, Longqiang Yu  and Shanghong Zhao

Information and Navigation College, Air Force Engineering University, Xi'an 710077, China

^{*} Correspondence: mq13909426684@163.com

Abstract: A novel photonic-assisted system for realizing the simultaneous measurement of Doppler frequency shift (DFS) and angle of arrival (AOA) is proposed. It is a simplified structure that is based on a dual-polarization dual-drive Mach–Zehnder modulator (DPol-DDMZM). The DFS direction can be accurately determined by comparing the phase relationship between the upper and lower low-frequency signal waveforms. An amplitude comparison function (ACF), which constructs a one-to-one mapping between the power ratio and the phase difference of echo microwave signals, can reduce the AOA measurement errors. The simulation results show that the simulated ACFs agree well with the theoretical ACFs, and the measurement errors of AOA are less than $\pm 2.8^\circ$ in a range of 0° to 78° . Moreover, the DFS can be realized by analyzing the spectrum of the low-frequency electrical signal with a measurement error of less than ± 0.05 Hz. The system structure is compact and cost-effective, which provides an alternative solution for modern radar and electronic warfare receivers.

Keywords: Doppler frequency shift; angle of arrival; microwave photonics; dual-parallel dual-dual Mach–Zehnder modulator



Citation: Meng, Q.; Lin, T.; Zhu, Z.; Wang, G.; Li, H.; Li, X.; Yu, L.; Zhao, S. Photonic Measurement for Doppler Frequency Shift and Angle of Arrival Based on a Dual-Polarization Dual-Drive Mach–Zehnder Modulator. *Photonics* **2022**, *9*, 666. <https://doi.org/10.3390/photonics9090666>

Received: 19 July 2022

Accepted: 15 September 2022

Published: 18 September 2022

Publisher's Note: MDPI stays neutral with regard to jurisdictional claims in published maps and institutional affiliations.



Copyright: © 2022 by the authors. Licensee MDPI, Basel, Switzerland. This article is an open access article distributed under the terms and conditions of the Creative Commons Attribution (CC BY) license (<https://creativecommons.org/licenses/by/4.0/>).

1. Introduction

Doppler frequency shift (DFS) and angle of arrival (AOA) measurement are widely investigated in radar [1], electronic warfare [2] and communication systems [3], mainly because the location, direction and radial velocity of moving targets can be judged by these two parameters. Conventional electrical-based DFS and AOA measurement technologies [4–6] suffer from bottlenecks such as electromagnetic interference and limited operation bandwidth. Therefore, to overcome the electronic bottleneck, microwave photonic measurement technologies for DFS and AOA are proposed and developed, which have the advantages of large working bandwidth, low loss, small size, and anti-electromagnetic interference.

Many photonic approaches for measuring the DFS [7–10] or the AOA [11–17] have been reported. These two parameters meet the requirement of velocity measurement and localization of the target objects, respectively. However, the structures of the measurement systems for these two parameters are independent of each other. This requires system reconstruction or multi-step operation to achieve simultaneous measurement of velocity and position. Recently, in order to solve the problem of multi-parameter measurement systems, some methods to simultaneously implement measurements of DFS and AOA based on one system have been proposed [18–24]. In [18], simultaneous measurements of AOA and DFS are accomplished by connecting a phase modulator (PM) and a polarization-division-multiplexed Mach–Zehnder modulator (PDM-MZM) in series. Moreover, an optical filter is needed to eliminate the undesired sidebands, which increases the system complexity and flexibility. In [19], only one dual-parallel Mach–Zehnder modulator (DP-MZM) is used in the structure, and two channels are built by separating the upper and the

lower sidebands through a wavelength-division multiplexer (WDM). It can realize the DFS measurement error of less than 0.07 Hz and the phase measurement error of less than 3.4° in the range of 300° without direction ambiguity. However, the usage of WDM limits the operating range of the system. In the systems of [20–22], unwanted frequency components are eliminated by setting the reference signal frequency 2 MHz above the transmitted signal frequency instead of using a WDM or a filter. These measurement systems are simple and compact. Nevertheless, the received echo signals and the local oscillator signal are difficult to synchronize, which will affect the measurement accuracy.

In this paper, we propose a photonic scheme to simultaneously implement the unambiguous measurement of the AOA and DFS utilizing an integrated dual-polarization dual-drive Mach–Zehnder modulator (DPol-DDMZM). An optical carrier is sent to the DPol-DDMZM. A transmitted signal is sent to one RF port of the sub-DDMZMs, and two echo signals are received by two antennas and are, respectively, fed into the other three RF ports of the two sub-DDMZMs. The modulated optical signals are demultiplexed by a polarization beam splitter (PBS) and divided into two branches. After photodetections (PDs), a pair of low-frequency electrical signals with a specific phase relationship is obtained. Here, an amplitude comparison function (ACF) which is a function of the power ratio between the two electrical signals is constructed, and the phase difference can be retrieved with the ratio of two detected microwave powers. Due to the monotonous relationship between the AOA and the phase difference, the unambiguous AOA can be realized in a range of 90° . The simulation results show that the AOA measurement error is less than $\pm 2.8^\circ$ in the range of 0° to 78° . Moreover, the value and the orientation of the DFS easily acquired by analyzing the spectrum of the low-frequency electrical signal with errors of less than ± 0.05 Hz. This system has a simple structure and does not require any optical filter or WDM, which makes the system operating frequency can be tuned flexibly. Therefore, it is more suitable for modern electronic warfare systems.

2. Principle

The proposed scheme for the simultaneous measurement of DFS and AOA is shown in Figure 1a. The echo signals are received by two antennas (Antenna 1 and Antenna 2), which are expressed as $V_{E1}(t) = V_e \exp(j\omega_e t)$ and $V_{E2}(t) = V_e \exp(j(\omega_e t + \phi))$, respectively. V_e , ω_e are the voltage and the angular frequency. ϕ is a phase difference between the two received signals. It is caused by a certain distance d between the two receiving antennas, which makes the echo signals have a certain time delay difference τ . The AOA of a microwave signal is defined as ϕ . The relationship between them can be given by

$$\phi = 2\pi f_e \tau \tag{1}$$

$$\phi = \sin^{-1}\left(\frac{\tau c}{d}\right) \tag{2}$$

where f_e is the frequency of the incoming echo signal, c is the velocity of electromagnetic radiation in the vacuum. Hence, the AOA can be expressed by the phase difference as

$$\phi = \sin^{-1}\left(\frac{\phi c}{2\pi f_e d}\right) \tag{3}$$

Doppler frequency shift (DFS) is defined as the frequency offset of the echo signal and the transmitted signal [25]. The moving object’s radial velocity and motor direction are commonly obtained from DFS, which can be written

$$v = \frac{c f_{DFS}}{2f_t} \tag{4}$$

where, f_{DFS} , f_t is the frequency of DFS and the transmitted signal, respectively.

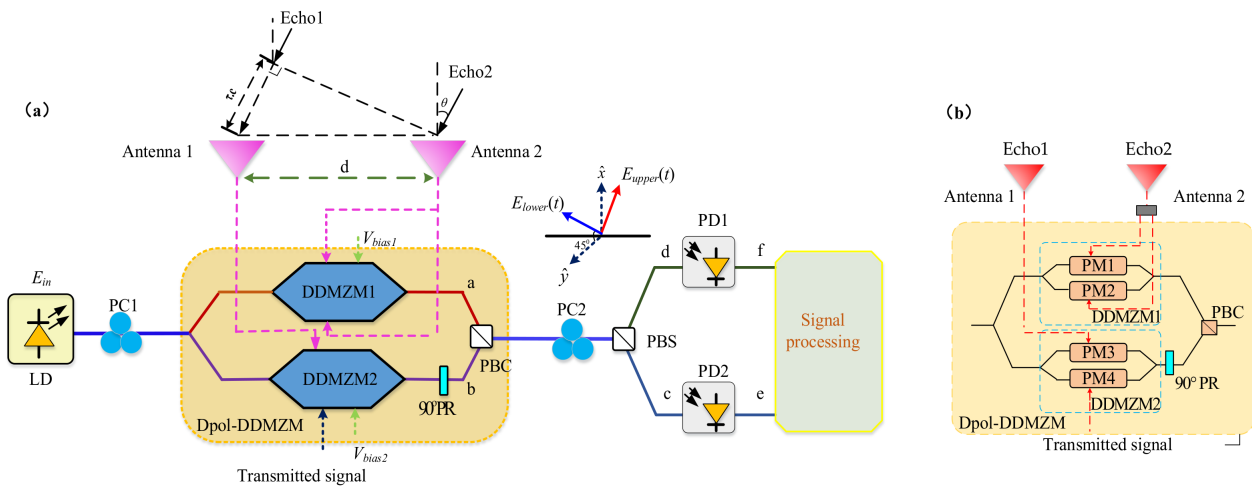


Figure 1. (a) Schematic diagram of the proposed AOA and DFS measurement system. LD: laser diode; DPol-DDMZM: dual-polarization dual-drive Mach–Zehnder modulator; PC: polarization controller; 90° PR: 90° polarization rotator; PBC: polarization beam combiner; PBS: polarization beam splitter; PD: photodetector. (b) The layout of DPol-DDMZM.

Referring to Figure 1a, an optical carrier generated from a laser diode (LD) is injected into a DPol-DDMZM via a polarization controller (PC1). It is expressed as $E_{in}(t) = E_c \exp(j\omega_c t)$, where E_c and ω_c are the amplitude and the angular frequency of the optical carrier. The echo1 received by antenna1 and transmitted microwave signal are sent to the two RF ports of DDMZM2, respectively. The echo2 received by antenna2 is divided by a splitter into two identical RF signals and sent to the two RF ports of DDMZM1, as shown in Figure 1b.

Two sub-DDMZMs both work at the maximum transmission point (MATP) to achieve phase modulation. Under the small-signal condition, the output signals of the DDMZM1 and the DDMZM2 can be expressed as:

$$E_{out1}(t) = \frac{E_{in} \sqrt{t_{ff}}}{4} \left[\sum_{n=-\infty}^{+\infty} 2(j^n J_n(m_e) \exp(jn\omega_e t)) \right] \tag{5}$$

$$= \frac{E_0 \exp(j\omega_c t) \sqrt{t_{ff}}}{4} [2(jJ_1(m_e) \exp(-j\omega_e t) + J_0(m_e) + jJ_1(m_e) \exp(j\omega_e t))]$$

$$E_{out2}(t) = \frac{E_{in} \sqrt{t_{ff}}}{4} \left[\sum_{n=-\infty}^{+\infty} j^n J_n(m_e) \exp(jn\omega_e t + jn\varphi) + \sum_{n=-\infty}^{+\infty} j^n J_n(m_t) \exp(jn\omega_t t) \right] \tag{6}$$

$$= \frac{E_0 \exp(j\omega_c t) \sqrt{t_{ff}}}{4} \left[(jJ_1(m_e) \exp(-j\omega_e t - j\varphi) + J_0(m_e) + jJ_1(m_e) \exp(j\omega_e t + j\varphi)) \right. \\ \left. + jJ_1(m_t) \exp(-j\omega_t t) + J_0(m_t) + jJ_1(m_t) \exp(j\omega_t t) \right]$$

where, t_{ff} is the insertion loss of the modulator, ω_e and ω_t are the angular frequency of the echo and transmitted microwave signal, respectively. $m_e = \pi V_e / V_\pi$ and $m_t = \pi V_t / V_\pi$ denote the modulation depth of the echo microwave signal and the transmitted microwave signal, respectively. V_t is the voltages of the transmitted microwave signal and V_π is the half-wave voltage of the sub-DDMZMs. $J_n(\cdot)$ is the Bessel function of the first kind of n-th order. Moreover, due to the following 90°PR in the lower arm, this modulator is a polarization multiplexed device. The output expression of the DPol-DDMZM can be written as

$$E_{out}(t) = \hat{x} E_{out1}(t) + \hat{y} E_{out2}(t) \tag{7}$$

where, \hat{x} and \hat{y} represent two orthogonal polarization states. Then the polarization multiplexed signal is rotated and aligned to one of the principal axes of the polarization beam

splitter (PBS) with the angle of 45° via a PC2. Thus, the optical signals along the upper branch and the lower branch of the PBS can be concluded as:

$$\begin{cases} E_{upper}(t) = \frac{\sqrt{2}}{2}[E_{out1}(t) - E_{out2}(t)] \\ E_{lower}(t) = \frac{\sqrt{2}}{2}[E_{out1}(t) + E_{out2}(t)] \end{cases} \quad (8)$$

Substituting Equations (5) and (6) into Equation (7), Equation (8) can be rewritten as:

$$\begin{cases} E_{upper}(t) = \frac{E_c \exp(j\omega_c t) \sqrt{t_{ff}}}{8} \begin{bmatrix} J_0(m_e) - J_0(m_t) + 2jJ_1(m_e)(\exp(-j\omega_e t) + \exp(j\omega_e t)) \\ -jJ_1(m_e)(\exp(-j\omega_e t - j\varphi) + \exp(j\omega_e t + j\varphi)) \\ -jJ_1(m_t)(\exp(-j\omega_t t) + \exp(j\omega_t t)) \end{bmatrix} \\ E_{lower}(t) = \frac{E_c \exp(j\omega_c t) \sqrt{t_{ff}}}{8} \begin{bmatrix} 3J_0(m_e) + J_0(m_t) + 2jJ_1(m_e)(\exp(-j\omega_e t) + \exp(j\omega_e t)) \\ +jJ_1(m_e)(\exp(-j\omega_e t - j\varphi) + \exp(j\omega_e t + j\varphi)) \\ +jJ_1(m_t)(\exp(-j\omega_t t) + \exp(j\omega_t t)) \end{bmatrix} \end{cases} \quad (9)$$

The output optical signals are detected separately by two low-speed photodetectors (PDs), and then the output photocurrents at the angular frequency of $\Delta\omega = |\omega_e - \omega_t|$ are as follows:

$$\begin{cases} I_{upper} = \frac{E_c^2 t_{ff}}{8} \eta J_1(m_e) J_1(m_t) \sqrt{A^2 + B^2} \cos((\omega_e - \omega_t)t - \arctan \frac{B}{A} - \pi) \\ I_{lower} = \frac{E_c^2 t_{ff}}{8} \eta J_1(m_e) J_1(m_t) \sqrt{C^2 + B^2} \cos((\omega_e - \omega_t)t + \arctan \frac{B}{C}) \end{cases} \quad \omega_e > \omega_t \quad (10)$$

$$\begin{cases} I_{upper} = \frac{E_c^2 t_{ff}}{8} \eta J_1(m_e) J_1(m_t) \sqrt{A^2 + B^2} \cos((\omega_t - \omega_e)t + \arctan \frac{B}{A} + \pi) \\ I_{lower} = \frac{E_c^2 t_{ff}}{8} \eta J_1(m_e) J_1(m_t) \sqrt{C^2 + B^2} \cos((\omega_t - \omega_e)t - \arctan \frac{B}{C}) \end{cases} \quad \omega_e < \omega_t \quad (11)$$

where, $A = 2 - \cos\varphi$, $B = \sin\varphi$, $C = \cos\varphi + 2$. As can be seen that the value of DFS, i.e., $\Delta f = |\omega_e - \omega_t|/2\pi$, can be figured out by processing the received electrical signals, and the moving direction of the target can also be distinguished by comparing the phase relationship of I_{upper} and I_{lower} . According to Equations (10) and (11), for the phase difference in the range of 0° to 180°, when the direction of the DFS is positive ($\omega_e > \omega_t$), the phase difference between I_{upper} and I_{lower} is from -180° to -234° . In contrast, the phase relationship between I_{upper} and I_{lower} is from 180° to 234° when the direction of the DFS is negative ($\omega_e < \omega_t$). Meanwhile, the phase of I_{lower} changes by inches with φ , but the phase of I_{upper} varies greatly with φ , as shown in Figure 2. Therefore, the direction of the DFS can be accurately determined.

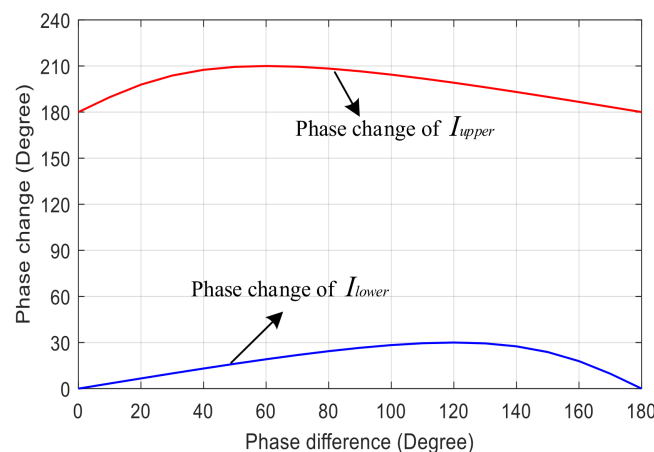


Figure 2. Phase change of I_{upper} and I_{lower} .

From Equation (10) or Equation (11), we can get the power of the frequency component that represents DFS frequency. It can be expressed as

$$\begin{cases} P_{upper} = \frac{E_c^4 t_{ff}^2}{8} \eta^2 J_1^2(m_e) J_1^2(m_t) (5 - 4 \cos \varphi) \\ P_{lower} = \frac{E_c^4 t_{ff}^2}{8} \eta^2 J_1^2(m_e) J_1^2(m_t) (5 + 4 \cos \varphi) \end{cases} \quad (12)$$

However, according to Equation (12), we can find that the output powers, both the upper branch and the lower branch are related to the carrier power and modulation indices. This means that the phase difference cannot be determined unless the input signal power of the carrier signal and the microwave signal are known, and this problem is appeared in the previously reported AOA measurement systems [14]. To solve this problem, amplitude comparison function (ACF) is introduced and given as the ratio between P_{upper} and P_{lower} .

$$ACF = \frac{P_{upper}}{P_{lower}} = \frac{5 - 4 \cos \varphi}{5 + 4 \cos \varphi} \quad (13)$$

As expressed in Equation (13), a one-to-one mapping between the power ratio and the phase difference of echo signals is obtained, as shown in Figure 3a. Furthermore, the incoming microwave signal phase difference is independent of the optical power and the input microwave power. It is obvious that when the power of the upper and lower branches is known, the phase difference can be calculated. Normally, the antenna separation is designed to be $d = \lambda/2$, where λ is the incoming RF signal wavelength, to avoid the grating lobes in the radiation pattern [26]. In this case, the AOA can be deduced from Equation (3) and the related numerical results are shown in Figure 3b. From Figure 3a, we can find that the phase shifts are symmetric between $0-180^\circ$ and $0-(-180^\circ)$ for ACF. Therefore, the system can realize the ambiguous phase measurement within the 180° phase range. The related AOA measurement range is from 0° to 90° .

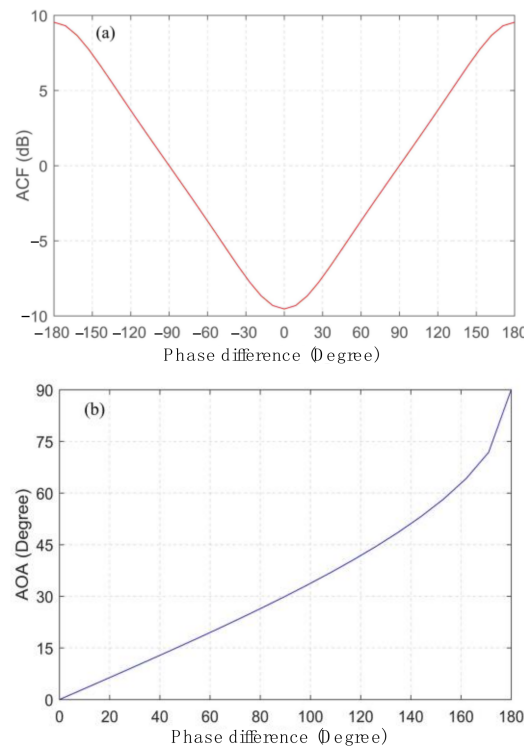


Figure 3. (a) Theoretically calculated ACF as the phase difference is changed from -180° to 180° . (b) The relationship between the AOA and phase shift within 180° .

3. Analysis and Simulation Results

To investigate its mechanism, simulations are performed via an OptiSystem 14.0. The setup can be found in Figure 1. An optical carrier with a wavelength of 1552.5 nm and a linewidth of 1 MHz is generated from a CW laser. It is equally split and injected into the DPol-DDMZM after a polarization controller (PC1). To imitate the scene where the DFS effect exists between the transmitted signal (reference signal) and the echo signals (echo1 signal and echo2 signal), two electrical signals are generated by two RF sources. A phase shifter is added to the echo1 signal to control the phase difference between the two echo signals. The echo1 signal and the transmitted signal are fed to two ports of DDMZM2, respectively. The echo2 signal is equally split into two signals by a power splitter and fed to two ports of DDMZM1. Following the DPol-DDMZM, a polarization controller (PC2) is used to rotate the polarization multiplexed signal to align to the two principal axes of a PBS. Then, the optical signal is polarization de-multiplexed into two branches. The outputs of the PBS are connected with two low-speed PDs with the responsivity of 1 A/W.

We set the transmitted signal frequency as 15 GHz with a power of 10 dBm. The echo microwave signal frequency is set to 15.002 GHz or 14.998 GHz with a power of 5 dBm. Therefore, a +2 MHz or −2 MHz of the DFS is generated, as shown in Figure 4a,b. It can be seen that the simulated DFS agrees well with the theoretical value. In order to check the accuracy of the simulation results of DFS, different DFSs are measured by tuning the frequency offset of the echo signal from −1 MHz to +1 MHz at intervals of 200 kHz, while the transmitted signal frequency is fixed at 15 GHz. The measured results are plotted in Figure 5. It can be seen that the measured values agree well with the theoretical ones, and the maximum DFS measurement error is within 0.05 Hz as well. When the DFS is 400 kHz and the frequency of the echo signals is 15 GHz, the error of radial velocity is less than 5×10^{-4} m/s according to Equation (4).

To validate the effectiveness of the AOA measurement, we can first achieve the phase difference and ACF mapping. Compared to the theoretical value according to Equation (13), it can be seen that the measured ACF agrees well with the theoretical value, as shown in Figure 6a for +2 MHz and Figure 6b for −2 MHz. Based on the measured value of ACF, the AOA can be deduced from Equation (3). As shown in Figure 6c for +2 MHz and Figure 6d for −2 MHz, the results denote a good AOA measurement ability that covers the range from 0° to 78°. The measurement errors of AOA are less than 2.8° in a range of 0° to 78° and the maximum error is less than 8° in a range of 79° to 90°. The reason for a large error around 90° is mainly due to the mathematical function relationship $\phi = \arcsin(\varphi/\pi)$ as $d = \lambda/2$, a small phase shift will bring a large change in AOA. In addition, comparing Figure 6c,d, we find that DFS has no effect on the measurement of AOA in this system.

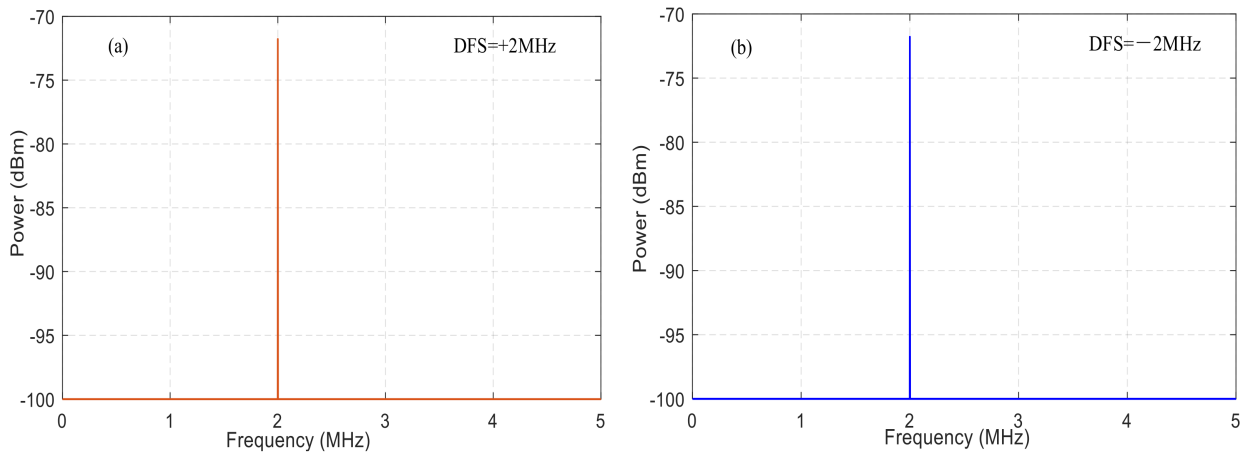


Figure 4. The electrical spectra in the upper branch for the DFSs at (a) +2 MHz and at (b) −2 MHz.

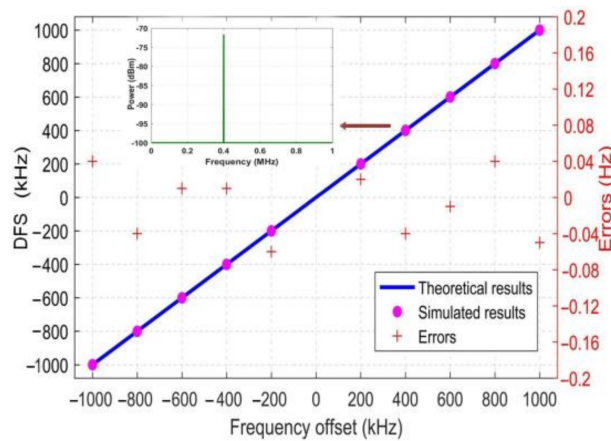


Figure 5. Measured different DFSs as the frequency offset of the echo signal from -1 MHz to $+1$ MHz at intervals of 200 kHz and the corresponding errors for the frequency of the transmitted signal at 15 GHz.

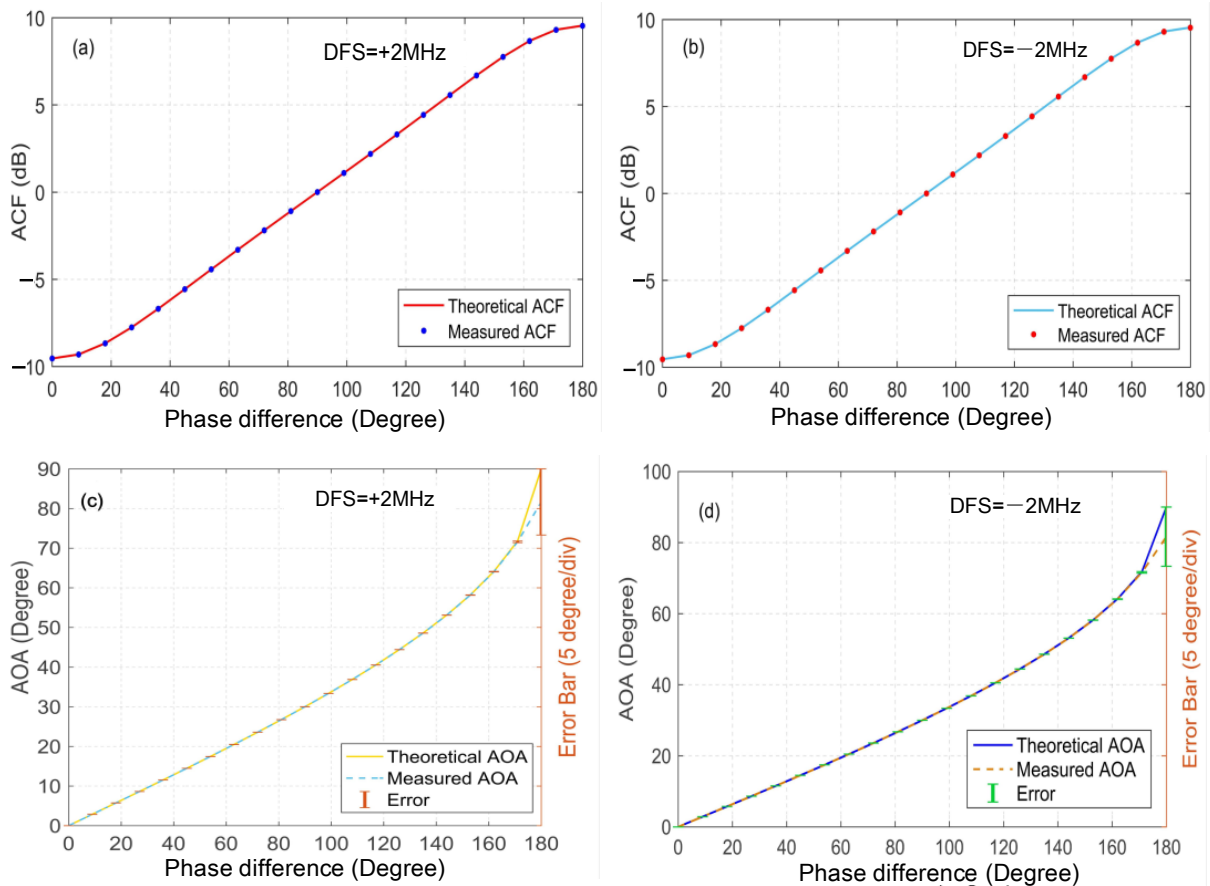


Figure 6. Comparison of the calculated value and the simulated value of ACF and AOA at different phase shifts. (a,c) for DFS = $+2$ MHz, (b,d) for DFS = -2 .

Subsequently, to clearly distinguish the direction of DFS, the signals of two channels are connected to a Dual Port RF Spectrum Analyzer to observe the phase relationship between the two signals as the phase difference in the range of 0° to 180° . Here, the phase difference between the echo signals of 0° , 60° , 90° , 120° , 160° and 180° are selected to observe the temporal waveforms when the DFS are $+2$ MHz and -2 MHz, as shown in Figure 7(a1–f1) and Figure 7(a2–f2), respectively. It is obvious that the phase relationship between I_{upper} and I_{lower} varies with the change of phase difference φ . As can be seen from

Figure 7(a1–f1), when the DFS is set to be +2 MHz, the phase relationship between I_{upper} and I_{lower} is from -180° to -234° , and the waveform of the upper path is advanced with respect to that of the lower one, which indicates that the direction of the DFS is positive. In contrast, from Figure 7(a2–f2) it can be found that the phase relationship between I_{upper} and I_{lower} is from 180° to 234° , and the phase in the upper branch is delayed with respect to that of the lower one when the DFS is set to be -2 MHz, which indicates that the direction of the DFS is negative. In addition, it can be found that the phase relation of the two channels is not blurred as the phase difference in the range of 0° to 180° , which means that the direction of DFS can be determined successfully and is not affected by the change of AOA.

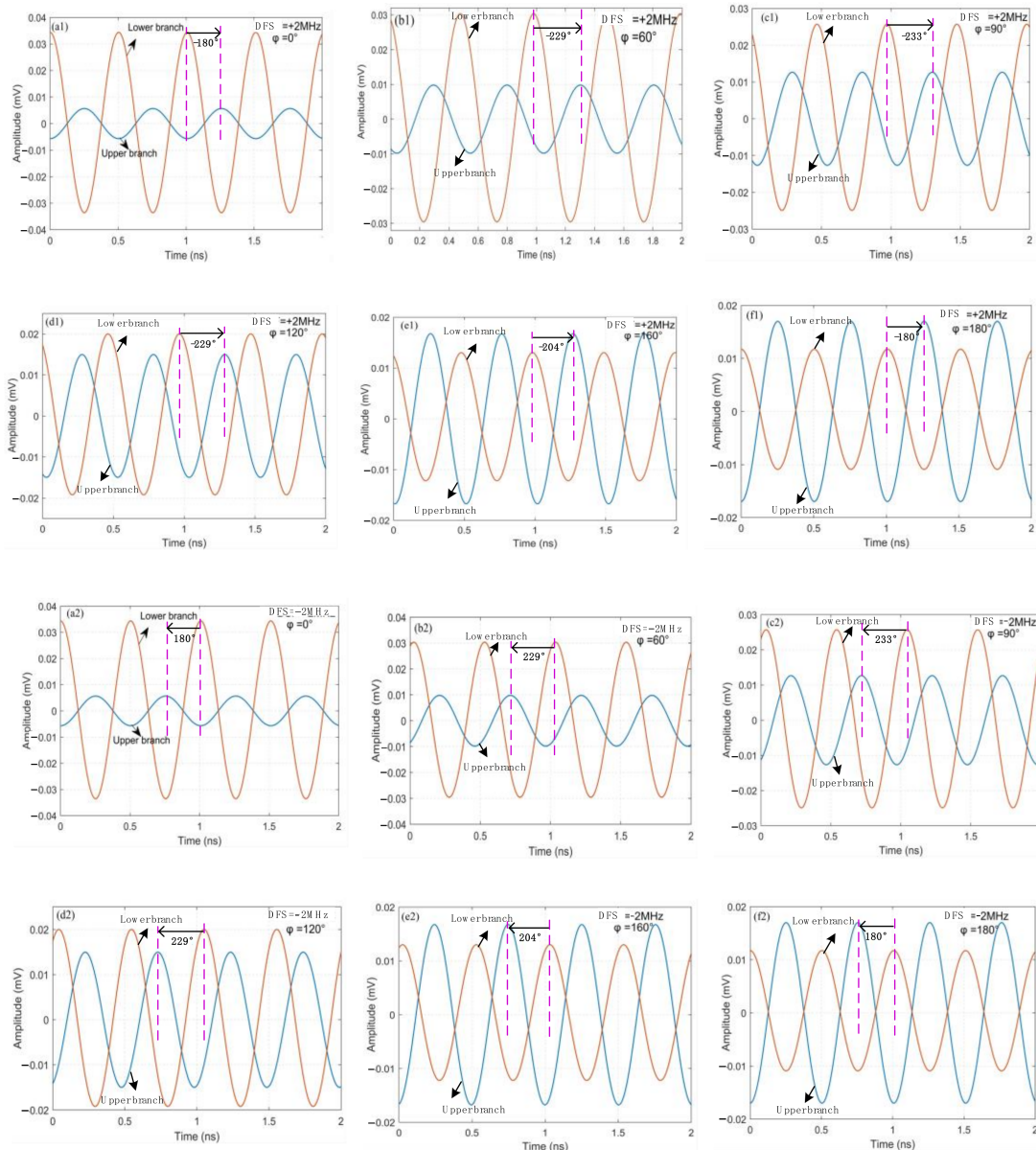


Figure 7. Waveforms of the upper branch and the lower branch for the DFS in different situations. (a1–f1) for the phase relationship between I_{upper} and I_{lower} when the DFS is +2 MHz and the phase difference between the echo signals is 0° , 60° , 90° , 120° , 160° and 180° , respectively. (a2–f2) for the phase relationship between I_{upper} and I_{lower} when the DFS is -2 MHz and the phase difference between the echo signals is 0° , 60° , 90° , 120° , 160° and 180° , respectively.

Some instability factors that may cause measurement errors, including the DC drift, the lower extinction ratio of two DDMZMs and phase shift caused by splitter, are also

considered and analyzed. Firstly, we assume that, α_1, α_2 are phase shifts introduced by the DC drift on DDMZM1 and DDMZM2, α_3 is a phase shift introduced by the splitter that is used to split the echo2 signal into two signals, a, b and c, d represent the amplitude imbalance caused by suboptimal extinction ratio of DDMZM1 and DDMZM2, respectively. The optical field output from the DDMZM1 and DDMZM2 can be rewritten as

$$\left\{ \begin{array}{l} E_{upper}(t) = \frac{E_0 \exp(j\omega_c t) \sqrt{t_{ff}}}{4} \begin{bmatrix} J_0(m_e)(ae^{-j\frac{\alpha_1}{2}} + be^{j(\frac{\alpha_1}{2} + \frac{\alpha_2}{2})} - ce^{j(\varphi - \frac{\alpha_3}{2})}) - dJ_0(m_t)e^{j\frac{\alpha_3}{2}} \\ + jJ_1(m_e) \exp(j\omega_e t)(ae^{-j\frac{\alpha_1}{2}} + be^{j(\frac{\alpha_1}{2} + \frac{\alpha_2}{2})} - ce^{j(\varphi - \frac{\alpha_3}{2})}) \\ + jJ_1(m_e) \exp(-j\omega_e t)(ae^{-j\frac{\alpha_1}{2}} + be^{j(\frac{\alpha_1}{2} + \frac{\alpha_2}{2})} - ce^{-j(\varphi + \frac{\alpha_3}{2})}) \\ - jJ_1(m_t)(\exp(-j\omega_t t) + \exp(j\omega_t t))(de^{j\frac{\alpha_3}{2}}) \end{bmatrix} \\ E_{lower}(t) = \frac{E_0 \exp(j\omega_c t) \sqrt{t_{ff}}}{4} \begin{bmatrix} J_0(m_e)(ae^{-j\frac{\alpha_1}{2}} + be^{j(\frac{\alpha_1}{2} + \frac{\alpha_2}{2})} + ce^{j(\varphi - \frac{\alpha_3}{2})}) + dJ_0(m_t)e^{j\frac{\alpha_3}{2}} \\ + jJ_1(m_e) \exp(j\omega_e t)(ae^{-j\frac{\alpha_1}{2}} + be^{j(\frac{\alpha_1}{2} + \frac{\alpha_2}{2})} + ce^{j(\varphi - \frac{\alpha_3}{2})}) \\ + jJ_1(m_e) \exp(-j\omega_e t)(ae^{-j\frac{\alpha_1}{2}} + be^{j(\frac{\alpha_1}{2} + \frac{\alpha_2}{2})} + ce^{-j(\varphi + \frac{\alpha_3}{2})}) \\ + jJ_1(m_t)(\exp(-j\omega_t t) + \exp(j\omega_t t))(de^{j\frac{\alpha_3}{2}}) \end{bmatrix} \end{array} \right. \quad (14)$$

After two PDs, the photocurrents are as follows:

$$\left\{ \begin{array}{l} I_{upper} \propto \frac{E_0^2 t_{ff}}{2} d J_1(m_e) J_1(m_t) \sqrt{A^2 + B^2} \cos((\omega_e - \omega_t)t - \arctan \frac{B}{A} - \pi) \\ I_{lower} \propto \frac{E_0^2 t_{ff}}{2} d J_1(m_e) J_1(m_t) \sqrt{C^2 + B^2} \cos((\omega_e - \omega_t)t + \arctan \frac{B}{C}) \end{array} \right. \quad \omega_e > \omega_t \quad (15)$$

$$\left\{ \begin{array}{l} I_{up} \propto \frac{E_0^2 t_{ff}}{2} d J_1(m_e) J_1(m_t) \sqrt{A^2 + B^2} \cos((\omega_t - \omega_e)t + \arctan \frac{B}{A} + \pi) \\ I_{down} \propto \frac{E_0^2 t_{ff}}{2} d J_1(m_e) J_1(m_t) \sqrt{C^2 + B^2} \cos((\omega_t - \omega_e)t - \arctan \frac{B}{C}) \end{array} \right. \quad \omega_e < \omega_t \quad (16)$$

where, $A = a \cos((\alpha_1 + \alpha_3)/2) + b \cos((\alpha_1 + \alpha_2 - \alpha_3)/2) - c \cos \alpha_3 \cos \varphi$, $B = c \cos \alpha_3 \sin \varphi$, $C = a \cos((\alpha_1 + \alpha_3)/2) + b \cos((\alpha_1 + \alpha_2 - \alpha_3)/2) + c \cos \alpha_3 \cos \varphi$. The power of the two electric signals can be given by

$$\left\{ \begin{array}{l} P_{upper} \propto \frac{E_0^4 t_{ff}^2}{4} d^2 J_1^2(m_e) J_1^2(m_t) [D^2 + c^2 \cos^2 \alpha_3 - 2Dc \cos \alpha_3 \cos \varphi] \\ P_{lower} \propto \frac{E_0^4 t_{ff}^2}{4} d^2 J_1^2(m_e) J_1^2(m_t) [D^2 + c^2 \cos^2 \alpha_3 + 2Dc \cos \alpha_3 \cos \varphi] \end{array} \right. \quad (17)$$

where, $D = a \cos((\alpha_1 + \alpha_3)/2) + b \cos((\alpha_1 + \alpha_2 - \alpha_3)/2)$. Equation (17) can be simplified as

$$\left\{ \begin{array}{l} P_{upper} \propto \frac{E_0^4 t_{ff}^2}{4} d^2 J_1^2(m_e) J_1^2(m_t) (I_0 - I_1 \cos \varphi) \\ P_{lower} \propto \frac{E_0^4 t_{ff}^2}{4} d^2 J_1^2(m_e) J_1^2(m_t) (I_0 + I_1 \cos \varphi) \end{array} \right. \quad (18)$$

where, $I_0 = D^2 + c^2 \cos^2 \alpha_3$, $I_1 = 2Dc \cos \alpha_3$. As a result, the amplitude comparison function (ACF) can be given by

$$ACF = \frac{P_{upper}}{P_{lower}} = \frac{I_0 - I_1 \cos \varphi}{I_0 + I_1 \cos \varphi} \quad (19)$$

As can be seen from Equations (15) and (16), these factors affect the phase difference and the amplitude of the two photocurrent signals, which means that the DFS and AOA measurement accuracy will be affected. Luckily, using ACF can reduce the impact factors for AOA on measurement according to Equation (19). The curves between the power ratio and the phase difference under different conditions are shown in Figure 8. Since α_1, α_2 both have similar effects on ACF, here we only drew a curve of α_1 . It can be seen from Figure 8a that the phase shifts introduced by the DC drift on DDMZM affect the ACF curve, which

means that it affects the value of phase difference. We also find that the ACF curve rotates around 90° , and the curve of α_1 deviation of 20° coincides with α_1 deviation of -20° , the same as 10° and -10° . Figure 8b shows the influence of α_3 deviation of $-20^\circ, -10^\circ, 0^\circ, 10^\circ$ and 20° , respectively. Conversely, α_3 causes the ACF curve to shift upward before 90° and downward after 90° . Compared with Ref. [12] using three DC biases, the proposed scheme only needs to control two DC biases, so the errors caused by DC drifts can be effectively reduced and the system is more stable.

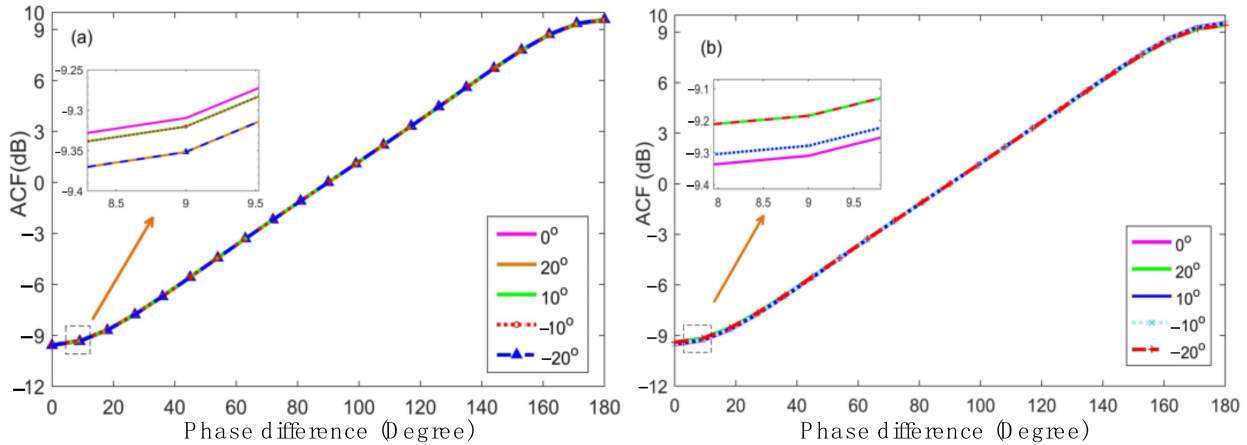


Figure 8. Slopes of ACFs versus different deviations of α_1 and α_3 . (a) The influence of α_1 deviation of $-20^\circ, -10^\circ, 0^\circ, 10^\circ$ and 20° , respectively. (b) The influence of α_3 deviation of $-20^\circ, -10^\circ, 0^\circ, 10^\circ$ and 20° , respectively.

In the above analysis, the polarization angle drift of PC2 is maintained at 45° . In practice, the angle will be influenced by environmental perturbation in the real system. Therefore, the impact of imperfect polarization angle is also considered. Here, we take the polarization angle as $\theta = 45^\circ + \Delta\theta$, the photocurrents from the two PDs are as follows:

$$\begin{cases} I_{upper} \propto \frac{E_0^2 t_{ff}}{4} J_1(m_e) J_1(m_t) \sqrt{A^2 + B^2} \cos((\omega_e - \omega_t)t - \arctan \frac{B}{A} - \pi) \\ I_{lower} \propto \frac{E_0^2 t_{ff}}{4} J_1(m_e) J_1(m_t) \sqrt{C^2 + B^2} \cos((\omega_e - \omega_t)t + \arctan \frac{B}{C}) \end{cases} \quad \omega_e > \omega_t \quad (20)$$

$$\begin{cases} I_{up} \propto \frac{E_0^2 t_{ff}}{4} J_1(m_e) J_1(m_t) \sin \theta \sqrt{A^2 + B^2} \cos((\omega_t - \omega_e)t - \arctan \frac{B}{A} - \pi) \\ I_{down} \propto \frac{E_0^2 t_{ff}}{4} J_1(m_e) J_1(m_t) \cos \theta \sqrt{C^2 + B^2} \cos((\omega_t - \omega_e)t + \arctan \frac{D}{C}) \end{cases} \quad \omega_e < \omega_t \quad (21)$$

where, $A = 2\cos\theta - \sin\theta\cos\varphi$, $B = \sin\theta\sin\varphi$, $C = 2\sin\theta + \cos\theta\cos\varphi$, $D = \cos\theta\sin\varphi$. The amplitude comparison function (ACF) can be derived as:

$$ACF = \frac{P_{upper}}{P_{lower}} = (\tan \theta)^2 \frac{4ctan\theta + \tan \theta - 4 \cos \varphi}{4 \tan \theta + ctan\theta + 4 \cos \varphi} \quad (22)$$

Figure 9 plots the impact of the polarization angle drift $\Delta\theta = 0^\circ, \pm 3^\circ, \pm 5^\circ$. It can be seen that the polarization angle drift can change the notch depth of the ACF curves, and curves intersect at the phase differences of 36° and 144° . It will influence the AOA measurement accuracy and the phase relationship between the upper branch and the lower branch for the DFS, but not the precise value of the DFS. In addition, although the phase relationship has changed between the upper branch and the lower branch, the direction of the DFS can still be accurately evaluated.

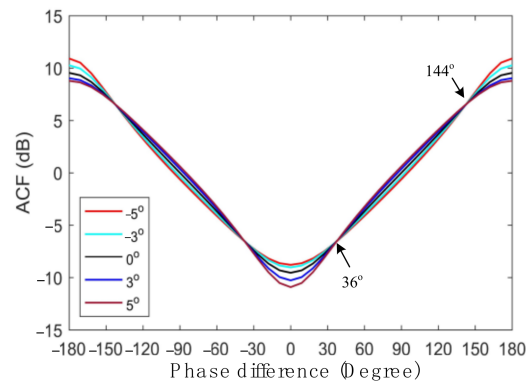


Figure 9. Slopes of ACFs versus different deviation of $\Delta\theta = 0^\circ, \pm 3^\circ, \pm 5^\circ$.

In order to improve the performance of the proposed scheme, integrated devices and a stable DC source can be used to reduce system instability. In addition, the polarization can also be stabilized by an electrical polarization controller or by using polarization-maintaining components.

4. Conclusions

We have proposed and analyzed a new photonic scheme that can simultaneously measure the DFS and AOA based on a DPol-DDMZM. The DFS can be acquired by measuring the frequencies of the two low-frequency electrical signals, and the DFS direction can be distinguished by comparing the phase relationship between the upper and lower branches. The simulation verifies that the DFS measurement error is less than ± 0.05 Hz. An amplitude comparison function (ACF) is established with a one-to-one mapping between the power ratio and the phase difference of echo microwave signals. The system has successfully achieved the measurement of AOA without ambiguity in the range of 90° . Based on the mathematical function relationship between phase difference and AOA, a small phase shift of phase difference around 180° will bring a large change in AOA. Therefore, it is good in the measurement range of 0° to 78° within 2.8° errors. There is a wide operation bandwidth in this measurement system because no filter or WDM is involved. Moreover, the proposed system structure is simple and compact, which is very promising for practical applications.

Author Contributions: Conceptualization, Q.M. and T.L.; methodology, G.W.; software, H.L.; validation, T.L., Z.Z. and H.L.; formal analysis, Z.Z.; investigation, H.L.; resources, Q.M.; data curation, G.W.; writing—original draft preparation, Q.M.; writing—review and editing, T.L.; visualization, X.L.; supervision, Q.M.; project administration, S.Z.; funding acquisition, X.L. and L.Y. All authors have read and agreed to the published version of the manuscript.

Funding: This research was supported in part by the National Natural Science Foundation of China (Grant No. 61901507), and in part by the Natural Science Foundation of Shaanxi Province (Grant No. 2020JQ-469).

Data Availability Statement: Not applicable.

Conflicts of Interest: The authors declare no conflict of interest.

References

- Chen, V.C.; Li, F.; Ho, S.S.; Wechsler, H. Micro-Doppler effect in radar: Phenomenon, model, and simulation study. *IEEE Trans. Aerosp. Electron. Syst.* **2006**, *42*, 2–21. [\[CrossRef\]](#)
- Khan, M.W.; Salman, N.; Kemp, A.H. Cooperative positioning using angle of arrival and time of arrival. In Proceedings of the 2014 Sensor Signal Processing for Defence (SSPD), Edinburgh, UK, 8–9 September 2014; pp. 1–5. [\[CrossRef\]](#)
- Zou, X.; Bai, W.; Chen, W.; Li, P.; Lu, B.; Yu, G.; Pan, W.; Luo, B.; Yan, L.; Shao, L. Microwave photonics for featured applications in high-speed railways: Communications, detection, and sensing. *J. Light. Technol.* **2018**, *36*, 4337–4346. [\[CrossRef\]](#)
- Rutkowski, A.; Stadnik, H. 2.45 GHz Band Quadrature Microwave Frequency Discriminators with Integrated Correlators Based on Power Dividers and Rat-Race Hybrids. *Electronics* **2021**, *10*, 2763. [\[CrossRef\]](#)

5. Rutkowski, A.K.; Kawalec, A. Two-dimensional portable short range of L band noise radar demonstrator. In Proceedings of the 2012 13th International Radar Symposium, Warsaw, Poland, 23–25 May 2012.
6. Rutkowski, A.; Kawalec, A. Some of Problems of Direction Finding of Ground-Based Radars Using Monopulse Location System Installed on Unmanned Aerial Vehicle. *Sensors* **2020**, *20*, 5186. [[CrossRef](#)] [[PubMed](#)]
7. Zou, X.; Li, W.; Lu, B.; Pan, W.; Yan, L.; Shao, L. Photonic Approach to Wide-Frequency-Range High-Resolution Microwave/Millimeter-Wave Doppler Frequency Shift Estimation. *IEEE Trans. Microw. Theory Tech.* **2015**, *63*, 1421–1430. [[CrossRef](#)]
8. Lu, B.; Pan, W.; Zou, X.; Pan, Y.; Liu, X.; Yan, L.; Luo, B. Wideband Microwave Doppler Frequency Shift Measurement and Direction Discrimination Using Photonic I/Q Detection. *J. Light. Technol.* **2016**, *34*, 4639–4645. [[CrossRef](#)]
9. Huang, C.; Chan, E.H.W.; Albert, C.B. Wideband DFS Measurement Using a Low-Frequency Reference Signal. *IEEE Photon. Technol. Lett.* **2019**, *31*, 1643–1646. [[CrossRef](#)]
10. Zhuo, H.; Wen, A.; Tu, Z. Photonic Doppler frequency shift measurement without ambiguity based on cascade modulation. *Opt. Commun.* **2020**, *470*, 125798. [[CrossRef](#)]
11. Cao, Z.; Wang, Q.; Lu, R.; Boom, H.P.A.V.D.; Tangdiongga, E.; Koonen, A.M.J. Phase modulation parallel optical delay detector for microwave angle-of-arrival measurement with accuracy monitored. *Opt. Lett.* **2014**, *39*, 1497–1500. [[CrossRef](#)]
12. Tu, Z.; Wen, A.; Xiu, Z.; Zhang, W.; Chen, M. Angle-of-Arrival Estimation of Broadband Microwave Signals Based on Microwave Photonic Filtering. *IEEE Photon. J.* **2017**, *9*, 5503208. [[CrossRef](#)]
13. Zhuo, H.; Wen, A.; Wang, Y. Photonic angle-of-arrival measurement without direction ambiguity based on a dual-parallel Mach–Zehnder modulator. *Opt. Commun.* **2019**, *451*, 286–289. [[CrossRef](#)]
14. Chen, H.; Chan, E.H.W. Simple Approach to Measure Angle of Arrival of a Microwave Signal. *IEEE Photon. Technol. Lett.* **2019**, *31*, 1795–1798. [[CrossRef](#)]
15. Chen, H.; Huang, C.; Chan, E.H.W. Photonic Approach for Measuring AOA of Multiple Signals with Improved Measurement Accuracy. *IEEE Photon. J.* **2020**, *12*, 7201810. [[CrossRef](#)]
16. Chen, H.; Chan, E.H.W. Photonics-Based CW/Pulsed Microwave Signal AOA Measurement System. *J. Light. Technol.* **2020**, *38*, 2292–2298. [[CrossRef](#)]
17. Huang, C.; Chan, E.H.W. Photonic Frequency Down Conversion Approach to Measure Microwave Signal Angle of Arrival. *IEEE Photon. J.* **2022**, *14*, 7226608. [[CrossRef](#)]
18. Li, P.; Yan, L.; Ye, J.; Feng, X.; Pan, W.; Luo, B.; Zou, X.; Zhou, T.; Chen, Z. Photonic approach for simultaneous measurements of Doppler-frequency-shift and angle-of-arrival of microwave signals. *Opt. Express* **2019**, *27*, 8709–8716. [[CrossRef](#)]
19. Zhuo, H.; Wen, A. A Photonic Approach for Doppler-Frequency-Shift and Angle-of-Arrival Measurement Without Direction Ambiguity. *J. Light. Technol.* **2021**, *39*, 1688–1695. [[CrossRef](#)]
20. Huang, C.; Chen, H.; Chan, E.H.W. Simple photonics-based system for Doppler frequency shift and angle of arrival measurement. *Opt. Express* **2020**, *28*, 14028–14037. [[CrossRef](#)]
21. Li, G.; Shi, D.; Wang, L.; Li, M.; Zhu, N.H.; Li, W. Photonic System for Simultaneous and Unambiguous Measurement of Angle-of-Arrival and Doppler-Frequency-Shift. *J. Light. Technol.* **2022**, *40*, 2321–2328. [[CrossRef](#)]
22. Cao, X.H.; Fan, X.J.; Li, G.Y.; Li, M.; Zhu, N.H.; Li, W. A Filterless Photonic Approach for DFS and AOA Measurement Using a Push-Pull DPoL-MZM. *IEEE Photon. Technol. Lett.* **2022**, *34*, 19–22. [[CrossRef](#)]
23. Zhao, J.; Tang, Z.; Pan, S. Photonic approach for simultaneous measurement of microwave DFS and AOA. *Appl. Opt.* **2021**, *60*, 4622–4626. [[CrossRef](#)] [[PubMed](#)]
24. Tang, L.; Tang, Z.; Li, S.; Liu, S.; Pan, S. Simultaneous Measurement of Microwave Doppler Frequency Shift and Angle of Arrival Based on a Silicon Integrated Chip. *IEEE Trans. Microw. Theory Tech.* **2022**, *70*, 4243–4251. [[CrossRef](#)]
25. Li, X.; Wen, A.; Chen, W.; Gao, Y.; Xiang, S.; Zhang, H.; Ma, X. Photonic Doppler frequency shift measurement based on a dual-polarization modulator. *Appl. Opt.* **2017**, *56*, 2084–2089. [[CrossRef](#)] [[PubMed](#)]
26. Chen, H.; Chan, E.H.W. Angle-of-Arrival Measurement System Using Double RF Modulation Technique. *IEEE Photon. J.* **2019**, *11*, 7200110. [[CrossRef](#)]